1 Supplementary Information for

2 **Excellent Thermomagnetic Power Generation for Harvesting Waste**

3 **Heat via a Second-order Ferromagnetic Transition**

4

5 *Haodong Chen, Xianliang Liu, Yao Liu, Longlong Xie, Ziyuan Yu, Kaiming Qiao,*

6 *Mingze Liu, Fengxia Hu, Baogen Shen, R. V. Ramanujan, Ke Chu, Hu Zhang*[*]

7

8 Haodong Chen, Xianliang Liu, Longlong Xie, Ziyuan Yu, Kaiming Qiao, Mingze Liu,

9 Prof. Hu Zhang

10 School of Materials Science and Engineering

11 University of Science and Technology of Beijing

12 Beijing 100083, P R China

13 E-mail: zhanghu@ustb.edu.cn

14

15 A.P. Yao Liu

16 Frontier Institute of Science and Technology

17 Xi'an Jiaotong University

18 Xi'an 710049, P R China

19 E-mail: liuyao12@xjtu.edu.cn

20

21 Prof. Fengxia Hu, Prof. Baogen Shen

22 Beijing National Laboratory for Condensed Matter Physics

23 Institute of Physics, Chinese Academy of Sciences

24 Beijing 100190, P R China

25 E-mail: fxhu@iphy.ac.cn; shenbg@iphy.ac.cn

26

27 Prof. R. V. Ramanujan

28 School of Materials Science and Engineering

[*]Corresponding author at: School of Materials Science and Engineering, University of Science and Technology

Beijing, Beijing, 100083, China. Tel.: +86-10-62333733.

E-mail address: zhanghu@ustb.edu.cn

1 Nanyang Technological University

2 Singapore 639798, Singapore

3 E-mail: Ramanujan@ntu.edu.sg

4

5 Prof. Ke Chu

6 School of Materials Science and Engineering

7 Lanzhou Jiaotong University

8 Lanzhou 730070, P R China

9 E-mail: chukelut@163.com

Supplementary Notes

Supplementary Note 1. Magnetization change rate *dM*/*dT*

Fig. S1 shows the magnetization change rate (*dM*/*dT*) derived from the *M−T* curves for (a) Co12.5, (b) Co14, and (c) NiMnIn, respectively. The *dM*/*dT* peak values of Co12.5, Co14, and NiMnIn alloys are 1.7 Am^2 kg^{-1} K^{-1}, 4.85 Am^2 kg^{-1} K^{-1}, and −1.78 Am^2 kg^{-1} K^{-1} during the heating process, and 1.34 Am^2 kg^{-1} K^{-1}, 3.61 Am^2 kg^{-1} K^{-1}, and −1.78 Am^2 kg^{-1} K^{-1} during the cooling process, respectively. For Co12.5 and Co14 alloys, the first-order magnetic transition (FOMT) results in a significant change of magnetization, but a distinct difference in the *dM*/*dT* peak values during heating and cooling can be observed, e.g., the difference between the *dM*/*dT* peaks during heating and cooling is as high as 27% for Co12.5 and 34% for Co14, respectively. Such a large difference is attributed to the thermal hysteresis accompanied with FOMT.

Thermal hysteresis of up to 14 K and 10 K is found during the FOMT martensitic transition for Co12.5 and Co14 alloys, respectively. This large thermal hysteresis not only causes the different *dM*/*dT* values, but also introduces variability in the operating temperature during heating and cooling, which causes difficulties in TMG design and degradation of TMG performance.[1-2] On the contrary, the second-order magnetic transition (SOMT) in NiMnIn alloy exhibits a perfectly reversible ferromagnetic (FM) to paramagnetic (PM) transition in the working temperature range without thermal hysteresis. The maximum *dM*/*dT* peak value of SOMT in NiMnIn alloy is even larger than the one of FOMT in Co12.5 alloy. This result indicates that the SOMT in NiMnIn alloy can have better TMG performance than that of FOMT in Heusler alloys.
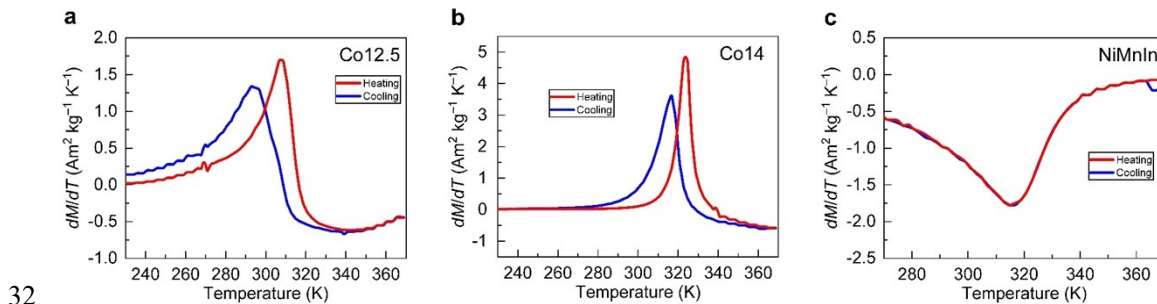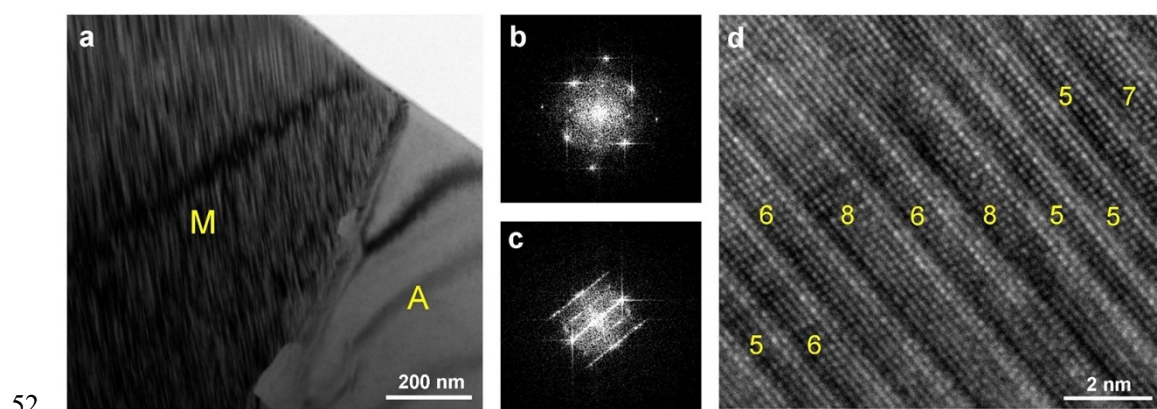

Fig. S1 The *dM*/*dT* derived from the *M−T* curves for (a) Co12.5, (b) Co14, and (c) NiMnIn, respectively.

Supplementary Note 2. Transmission electron microscopy of Co14

To gain deeper insights into the microstructure of the Heusler alloys with a first-order ferromagnetic martensitic transition around room temperature, transmission electron microscopy (TEM) was carried out. Fig. S2a shows the bright-field TEM image of Co14 alloy at room temperature. Fig. S2b and S2c show the fast Fourier transform (FFT) patterns for the regions A and M, respectively. These FFT patterns indicate that the phases in regions A and M are austenite and martensite, respectively. This result reveals that both martensite and austenite phases coexist in Co14 alloy at room temperature, confirming that the first-order ferromagnetic martensitic transition occurs around room temperature.

Fig. S2d displays the high-resolution transmission electron microscopy (HRTEM) image for the martensite phase. It is seen that the martensite shows a specific stacking-mediated structure with locally different stacking periodicities at nano scale, which confirms the modulated structure of the martensite, and this finding is consistent with the XRD analysis. Each stacking periodicity is composed of different number of atomic layers. The formation of the stacking-mediated structure is attributed to the similar free energies of the martensites with different stacking periodicities.[3]

Fig. S2 (a) Bright-field image for an area with coexisting austenite and martensite in the Co14 alloy. (b) Fast Fourier transform (FFT) pattern for the region A. (c) FFT pattern for the region M. (d) High-resolution transmission electron microscopy (HRTEM) image for martensite. The numbers represent the number of atomic layers contained in each stacking periodicity.

59 Supplementary Note 3. Magnetocaloric effect (MCE)

60   Fig. S3a and S3b show the isothermal magnetization ($M-H$) curves for Co12.5 and

61 Co14 alloys around their FOMT. Fig. S3c shows the $M-H$ curves for NiMnIn around

62 its SOMT. The magnetization of both Co12.5 and Co14 alloys increases with increasing

63 temperature. With higher field they experience a field-induced metamagnetic transition

64 from the weak magnetic state to the FM state with a distinct magnetic hysteresis around

65 the martensitic transition temperature, confirming that it is a FOMT.

66   On the other hand, the magnetization of NiMnIn decreases with an increase of

67 temperature around its T_C. Below the T_C, the magnetization increases rapidly at low

68 fields and tends to saturate with increasing field, corresponding to typical FM behavior.

69 Above the T_C, the magnetization increases linearly with higher field, indicating a PM

70 state. Moreover, no magnetic hysteresis is observed in these isotherms. The above facts

71 reveal that the NiMnIn undergoes a SOMT from the FM to the PM states.
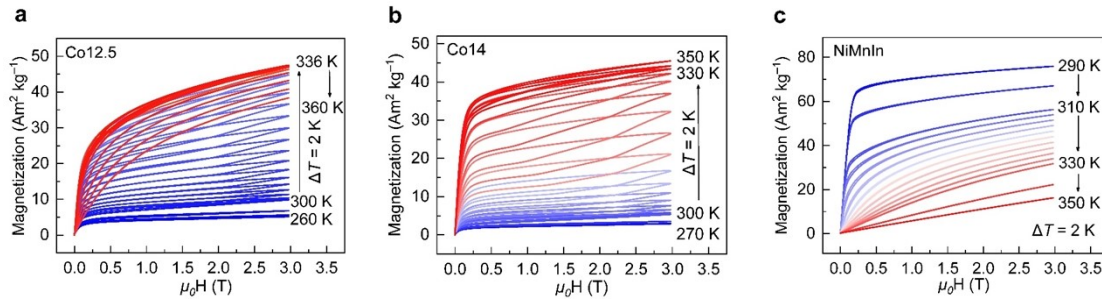
72

73 **Fig. S3** The isothermal magnetization ($M-H$) curves near the martensitic transition for (a) Co12.5,
74 (b) Co14, and near the T_C for (c) NiMnIn, respectively.

75   Based on the above magnetization isotherms, the ΔS_M values for various magnetic

76 field changes were calculated by the Maxwell relationship:[4]

$$\Delta S_M (T,H) = \mu_0 \int_0^H \left(\frac{\partial M}{\partial T} \right)_H dH \tag{S1}$$

78 where μ_0 is the permeability of vacuum. In practice, the ΔS_M value can be calculated

79 using the following numerical approximation:

$$\Delta S_M (T,H) = \mu_0 \sum_i \frac{M_{i+1} - M_i}{T_{i+1} - T_i} \Delta H_i \tag{S2}$$

81 where M_i and M_{i+1} are the magnetization values at temperatures of T_i and T_{i+1} when the

82   magnetic field is H_i, respectively, and ΔH_i is the change of the magnetic field.

83   Fig. S4 shows the temperature dependence of ΔS_M under different magnetic field

84   changes up to 3 T for Co12.5 and Co14 alloys around their FOMT and NiMnIn around

85   its SOMT. Both Co12.5 and Co14 alloys show a sharp positive ΔS_M peak due to the

86   FOMT, and the peak ΔS_M value for a field change of 3 T is 4.17 J kg^{-1} K^{-1} for Co12.5

87   and 7.66 J kg^{-1} K^{-1} for Co14, respectively. An increase in Co content in a Ni-Mn-Ti

88   based alloy would strengthen the first-order martensitic transition,[5] leading to higher

89   ΔS_M as well as a narrower peak for Co14 alloy. In addition, a small negative ΔS_M is

90   found after the positive ΔS_M peak in both alloys, which is attributed to the SOMT of

91   austenite.[6]

92   In comparison, NiMnIn shows a wider negative ΔS_M peak around its T_C. Usually,

93   the ΔS_M of SOMT is much lower than that of FOMT. However, the ΔS_M of SOMT in

94   NiMnIn is comparable to that of FOMT in Co12.5 and Co14 alloys, and it is even higher

95   than those of Co12.5 and Co14 alloys at low magnetic fields. For example, the $|\Delta S_M|$

96   peak of NiMnIn reaches 2.37 J kg^{-1} K^{-1} under 1 T, which is 2.21 and 1.06 times that of

97   Co12.5 (1.07 J kg^{-1} K^{-1}) and Co14 (2.23 J kg^{-1} K^{-1}).

98   The maximum field supplied by permanent magnets is usually lower than 2 T.

99   Therefore, it is desirable to search for materials with high MCE and TMG performance

100   under low magnetic field. This large MCE of SOMT in NiMnIn under low magnetic

101   fields suggests better TMG performance than that of the FOMT in Co12.5 and Co14

102   alloys, satisfying the above requirement and displaying high potential for practical

103   applications.
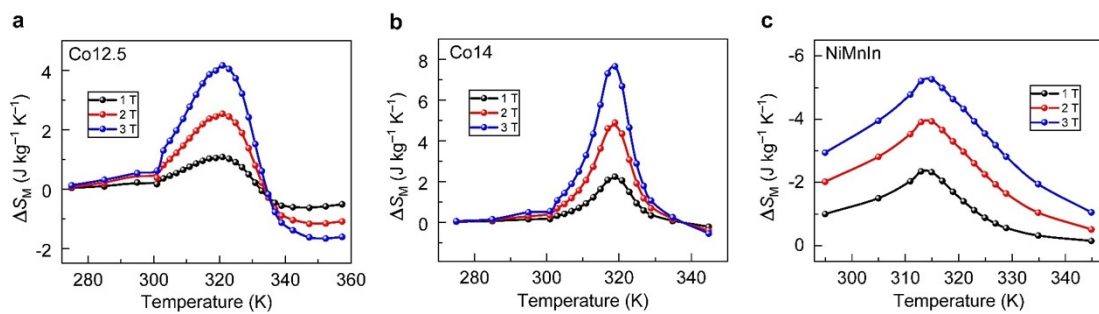
104

105   **Fig. S4** Temperature dependence of ΔS_M under different magnetic field changes up to 3 T for (a)
106   Co12.5, (b) Co14 alloys around their FOMT and (c) NiMnIn around its SOMT.

Supplementary Note 4. Thermal properties of Heusler alloys

4.1 Heat capacity (C_P) and thermal conductivity (λ)

Fig. S5 shows the temperature dependence of the heat capacity C_P under 1 T for (a) Co12.5, (b) Co14, and (c) NiMnIn, respectively. A C_P peak appears around their respective transition temperature. However, the Co12.5 and Co14 alloys show large thermal hysteresis due to the FOMT, resulting in different C_P values during heating and cooling. Such a difference in C_P values would cause differences in the rate of temperature change dT/dt as well as the TMG performance during heating and cooling process.

In comparison with above alloys, NiMnIn alloy has a lower C_P value with a maximum value of 650 J kg^{-1} K^{-1} near its T_C, which would enhance the dT/dt. Moreover, there is no thermal hysteresis during the heating and cooling process, ensuring the consistency of working temperature and TMG performance during cycling.
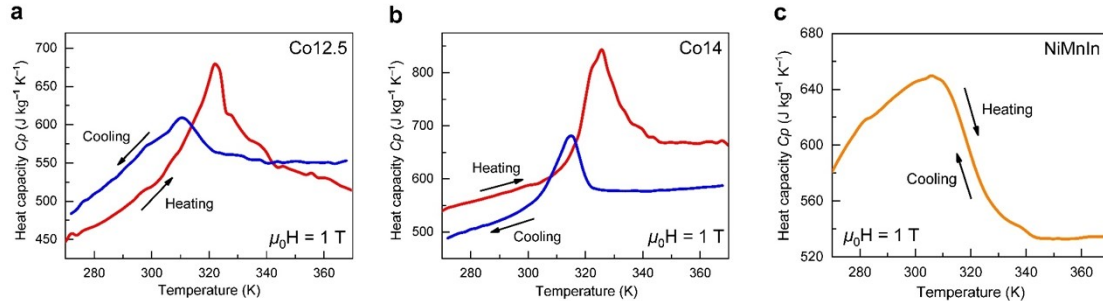
Fig. S5 Temperature dependence of heat capacity C_P under 1 T for (a) Co12.5, (b) Co14, and (c) NiMnIn, respectively.

Fig. S6 compares the temperature dependence of thermal conductivity λ for all the samples. The average thermal conductivity λ_{ave} of Co12.5, Co14 and NiMnIn alloys are 9.56 W m^{-1} K^{-1}, 9.39 W m^{-1} K^{-1}, and 14.86 W m^{-1} K^{-1}, respectively. NiMnIn alloy has the highest λ_{ave} value, which is 1.55 and 1.58 times that of Co12.5 and Co14 alloys, respectively. This result indicates that NiMnIn alloy has the best heat transfer capability, which is also favorable for high TMG performance.

130
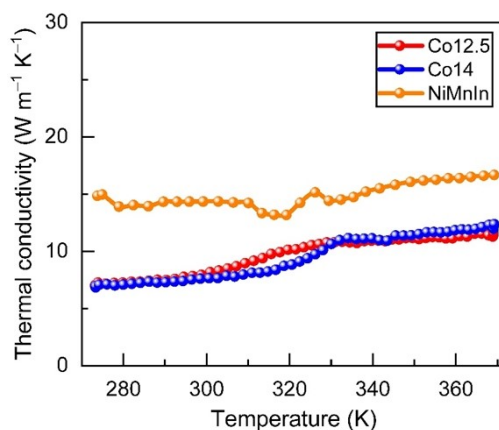
Fig. S6 Temperature dependence of thermal conductivity λ for Co12.5, Co14, and NiMnIn alloys.

Our recent work reveals that the C_P and λ affect the TMG performance largely, e.g., 10% change rate of C_P and λ would cause 2~4% change rate of induced current I.[7] Here, the C_P of NiMnIn is ~30% lower than the maximum C_P of Co14, and the λ is ~58% higher than the maximum λ of Co14 alloy. Therefore, the induced current I of NiMnIn alloy would be probably 18%~36% higher than that of Co14 alloy. The calculated result based on the experiential current shows that the I_{max} of NiMnIn alloy is 25.5% higher than that of Co14 alloy, consistent with above prediction. Besides, the following study confirms that the I_{max} of 286.6 μA g^{-1} generated by NiMnIn in present work is 1–4 orders of magnitude higher than those of other works. To our knowledge, this is the highest I_{max} reported so far.

4.2. Calculation of average temperature (T_{ave})

A thermocouple was attached to the sample surface to measure the temperature change, Fig. 1e in the main paper shows the variation of measured temperature during the heating and cooling cycling. The water temperature shows a steady cyclic change between the hot-end and cold-end. The water temperature in the copper cabin reaches ~289 K (cold-end) and ~369 K (hot-end) after passing through the pump and pipe; the working temperature range of the TMG device is suitable for harvesting low-grade waste heat. However, there is a temperature gradient from the surface to the center of bulk sample. The isometric segmentation method[2] was used to calculate the average sample temperature.
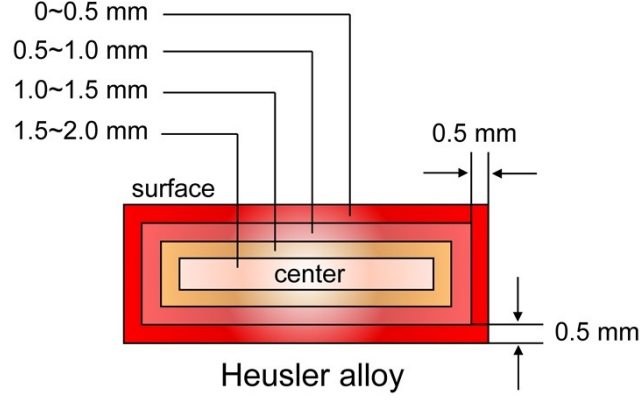
Fig. S7 Schematic diagram of the isometric segmentation method.

As shown in Fig. S7, the sample was divided with equal intervals of 0.5 mm from the surface to the center, the temperature of each part can be calculated using the following equations:[2]

$$\alpha = \frac{\lambda}{\rho C_P} \tag{S3}$$

$$\eta = \frac{z}{2\sqrt{\alpha t}} \tag{S4}$$

$$\frac{T(z,t) - T_c}{T_h - T_c} = 1 - \frac{2}{\sqrt{\pi}} \int_0^\eta e^{-\tau^2} d\tau \tag{S5}$$

where $T(z,t)$ is the temperature at time t, z is the distance from the sample surface, C_P is the heat capacity (Fig. S5), λ is the thermal conductivity (Fig. S6), ρ is the density of the sample, τ is the time interval of 0.3 s, T_c is the cold-end temperature (289 K) and T_h is the hot-end temperature (369 K).

Fig. S8 shows the calculated temperature of each part with time for Co12.5, Co14, and NiMnIn alloys, respectively. The temperature varies gradually from the surface to the center, confirming the existence of a temperature gradient in the bulk sample. Since the outermost layer contacts with the hot and cold fluids directly, the surface temperature changes much faster than the center temperature. The calculated temperature of the sample surface (0~0.5 mm) is consistent with the measured surface temperature (dash line), which verifies the calculation method. Then the average temperature of the bulk sample can be calculated using the equation:

$$172 \qquad\qquad T_{\text{ave}}(t) = \sum_{i=1}^{5} T_i(t)\frac{V_i}{V} \qquad\qquad\qquad (S6)$$

173 where $T_i(t)$ is the temperature of part i, V_i and V are the volumes of part i and the whole

174 sample, respectively. The average temperature of the bulk sample is plotted as a dotted

175 dash line in Fig. S8.
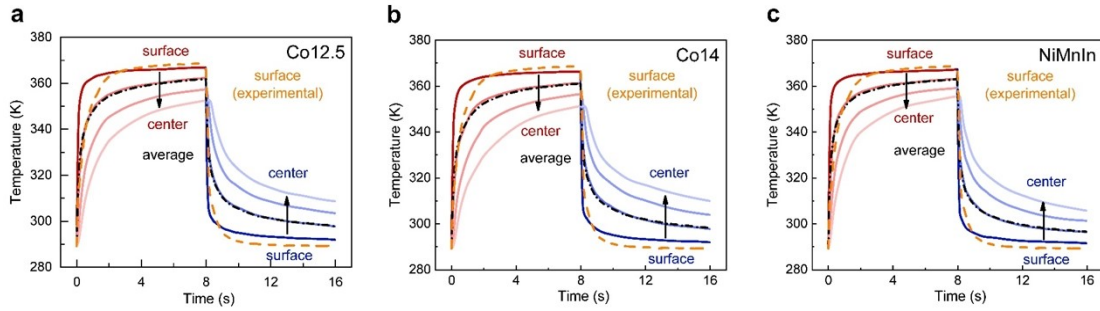
176

177 **Fig. S8** The calculated temperature of each part with time for (a) Co12.5, (b) Co14, and (c) NiMnIn,

178 respectively.

179   Fig. S9a shows the calculated T_{ave}–t curves during one cycle for all the samples.

180 The T_{ave} rises sharply from 289 K to ~350 K within the first 2 s due to the large

181 temperature difference between the heating fluid and the sample. As the temperature

182 difference decreases, the T_{ave} rises slowly and reaches ~360 K at 8 s. Similarly, T_{ave}

183 drops drastically in the beginning during cooling, and then T_{ave} decreases slowly and

184 reaches ~360 K at 16 s. Due to the large thermal hysteresis of FOMT, the transition

185 temperatures occur at different temperatures during heating and cooling for the Co12.5

186 and Co14 alloys, which is undesirable. Moreover, the reverse transition from austenite

187 to martensite cannot be completed during cooling within the TMG temperature range

188 in the Co12.5 alloy due to thermal hysteresis. This incomplete transition would cause a

189 lower induced power during the cooling. In contrast, the T_C of SOMT in NiMnIn

190 remains constant during the heating and cooling processes. In addition, due to the low

191 C_P and high λ, NiMnIn alloy shows the fastest temperature change among all the

192 samples, which is favorable to obtaining large TMG performance.
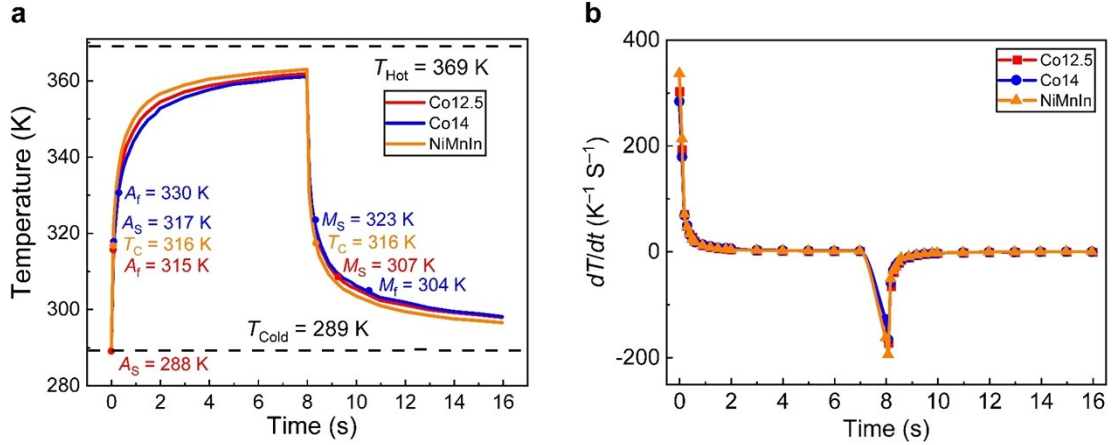
Fig. S9 (a) The calculated average sample temperature during one cycle for Co12.5, Co14, and NiMnIn, respectively. (b) The temperature change rate (dT/dt) derived from the $T−t$ curves for Co12.5, Co14, and NiMnIn, respectively.

Fig. S9b shows the corresponding temperature change rate (dT/dt) derived from the $T_{ave}–t$ curves for all the alloys. The dT/dt peaks of Co12.5, Co14, and NiMnIn alloys are 302.4 K^{-1} S^{-1}, 284.2 K^{-1} S^{-1}, and 336.9 K^{-1} S^{-1} during the heating process, and −172.3 K^{-1} S^{-1}, −166.9 K^{-1} S^{-1}, and −195.2 K^{-1} S^{-1} during the cooling process, respectively. NiMnIn alloy has the fastest temperature change rate dT/dt among all the alloys. Besides, the dT/dt values during heating are much higher than the corresponding values during cooling. The initial sample temperature is 289 K and it is uniform for bulk samples. However, the sample temperature cannot be uniform after the first heating process due to the temperature gradient. The average sample temperature after cooling would be higher than the initial temperature, as shown in Fig. S9a. Our recent work showed that the higher cold-end temperature would lower the dT/dt,[8] which leads to lower dT/dt during cooling for all the samples.

4.3. Calculation of average magnetization

The magnetization of each part can be obtained according to the $M–T$ curves (Fig. 2b-2d) and the $T–t$ curves (Fig. S8). Fig. S10 shows the calculated magnetization of each part as a function of time. For Co12.5 and Co14 alloys, the magnetization during heating increases rapidly at first, corresponding to the FOMT from weak magnetic martensite to FM austenite. Then, the magnetization decreases slowly due to the SOMT from the FM to the PM states. During the cooling process, the magnetization increases

11

216 fast in the beginning due to the reversible SOMT, followed by a gradual decrease of

217 magnetization, which is attributed to the FOMT from FM austenite to a weak-magnetic

218 martensite. It is noted that, although the ΔM during the SOMT is lower than the one

219 during the FOMT, the faster dT/dt at the beginning of cooling makes a faster change of

220 magnetization during the SOMT than the one during the followed FOMT. Hence,

221 unlike the MCE, which is mainly related to dM/dT, dT/dt also plays an important role

222 in the TMG according to $V \propto (dM/dT)(dT/dt)$.

223   The magnetization of the surface changes faster than that of the interior, which is

224 also due to the faster temperature change of the surface, as shown in Fig. S8. For

225 NiMnIn, it experiences a reversible SOMT during the heating and cooling processes,

226 but the average magnetization changes faster during heating than during cooling. The

227 $T_C = 316$ K of NiMnIn is closer to the cold-end temperature (289 K), and so the

228 magnetic transition occurs earlier during heating than cooling. Accordingly,

229 magnetization changes faster at the beginning of the heating process.
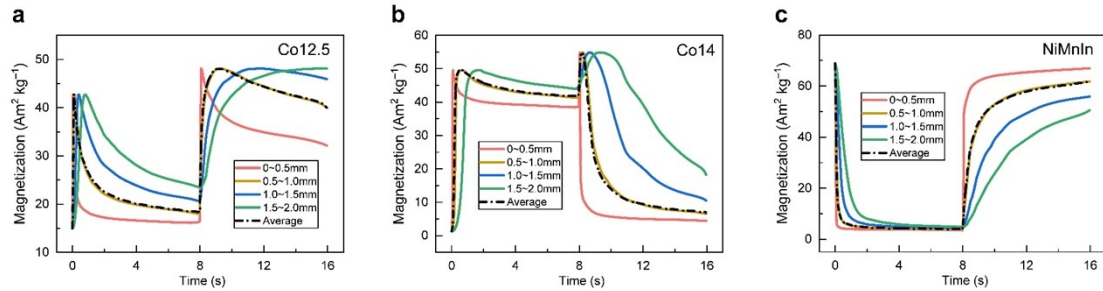
230

231 **Fig. S10** The calculated magnetization of each part as a function of time for (a) Co12.5, (b) Co14,

232 and (c) NiMnIn, respectively.

233 ## 4.4 Heat transfer during TMG operation

234   Fig. S11 shows the infrared heat map of the copper cabin and the water pipe during

235 heating and cooling. During the heating process (Fig. S11a), the copper cabin and the

236 sample absorb heat from the hot water, hence, the temperature of the outlet pipe (M3:

237 350.2 K) is lower than that of inlet pipe (M1: 353.2 K). On the contrary, the cold water

238 removed heat from the copper cabin and the sample during the cooling process (Fig.

239 S11b), causing the temperature of the outlet pipe (M3: 302.5 K) to be slightly higher

240 than that of the inlet pipe (M1: 300.7 K).

241   The heat absorbed or released by water Q_{water} can be expressed by the following

242 equation:

$$Q_{water} = cm(T_2 - T_1) \tag{S7}$$

244 where c is the specific heat capacity of water, m is the mass of the water flowing through

245 the copper cabin, and T_1, T_2 are the initial and final temperatures of water. The heat

246 released by water during heating is 4.03 kJ, and the absorbed heat during cooling is

247 2.42 kJ, which is lower than the released heat during heating. This fact indicates that a

248 certain amount of residual heat remains in the sample cabin and is not absorbed by cold

249 water during cooling, which would then lower the dT/dt during cooling.

250   In addition, the copper cabin temperature (M2) is lower or higher than the pipe

251 temperatures (M1, M3). This is likely due to the shielding of the thermal radiation of

252 the sample cabin during the measurement of infrared camera. To visually display the

253 temperature change of each water pipe during heating and cooling, we attached Nos. 1,

254 2, and 3 temperature patches on the cold water pipe, hot water pipe, and common pipe,

255 respectively. The color change of the temperature patch on each pipe is shown in the

256 inset of Fig. S11.

257
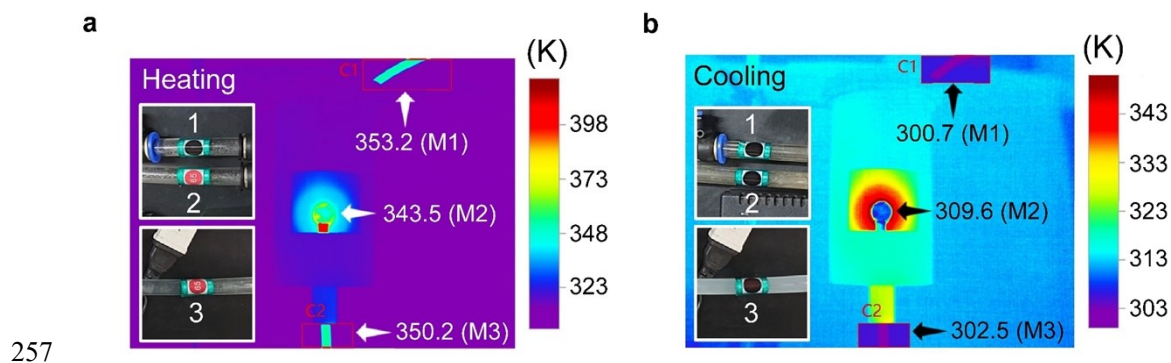
258 **Fig. S11** Temperature change of the copper cabin and water pipe during (a) heating and (b) cooling
259 process photographed by infrared thermal imager. The inlet pipe (C1) and outlet pipe (C2) areas
260 had been temperature corrected. The inset shows the color change of temperature patch on the cold
261 water pipe (1), hot water pipe (2), and confluent pipe (3), respectively.

262   When the temperature exceeds 338 K, the temperature patch will change from

263 black to red. Pipe (1) is the cold water pipe, and it is always black. Pipe (2) is the hot

264 water pipe, which turns to red when hot water is pumped through it. The confluent pipe

265 (3) flows hot and cold water alternately during the heating and cooling processes, so it

266 alternately turns red and black.

Supplementary Note 5. The induced voltage V within 300 s

Fig. S12 shows the experimental voltage generated by our TMG device within 300 s for all the alloys. Both Co12.5 and Co14 alloys produce two V peaks in each heating/cooling cycle due to the successive FOMT and SOMT, while NiMnIn only generates one V peak generated by SOMT. All the alloys generate AC electricity during the continuous cycles, suggesting the stable power generation performance of our TMG.

The total voltage (V_{tol}) within 300 s for Co12.5, Co14, and NiMnIn are 1.82, 2.68, and 2.68 V g^{-1}, respectively. Although the TMG property is only contributed by the SOMT in NiMnIn rather than Co12.5 and Co14 in which both FOMT and SOMT contribute to the TMG property, NiMnIn shows the highest V_{tol} among all the alloys.
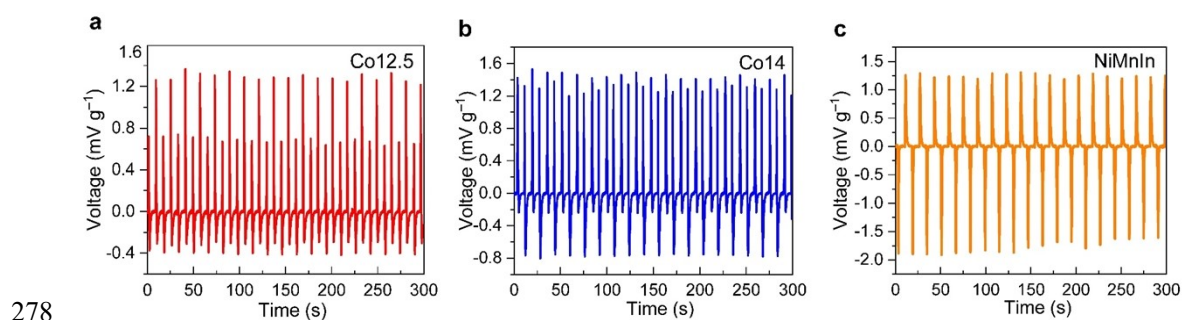
Fig. S12 The experimental induced voltage within 300 s for (a) Co12.5, (b) Co14, and (c) NiMnIn, respectively.

Supplementary Note 6. Finite element simulation

The TMG performance of the studied alloys was also investigated using finite element simulations by the COMSOL Multiphysics software (Version 5.4). The magnetic field (MF) module as well as solid and fluid heat transfer module (HT) in AC/DC were selected, and then the simulation process was carried out by the following steps:

Step 1: Build the model of the device with the size parameters as input (Table S1).

Step 2: Input the parameters of the TMG materials including density (in the "Methods" section), change of magnetization with temperature (Fig. 2b-2d), heat capacity (Fig. S5), thermal conductivity (Fig. S6), and the parameters of the permanent

291 magnet (Table S1).

292   Step 3: Employ the heat transfer module of COMSOL to simulate the variation of

293 sample temperature during the cycling, i.e., T–t curves.

294   Step 4: Employ the magnetic field module to calculate the value of B as a function

295 of time based on the above simulated T–t curves and the experimental M–T curves (Fig.

296 2b-2d).

297   Step 5: The COMSOL simulates the induced voltage V based on the rate of change

298 of B according to equation (1) in the main text.

Supplementary Note 7. The experiment of lighting up the LEDs

300   By utilizing this high TMG performance, we successfully lit up the commercial

301 LEDs using our TMG device. Fig. S13 shows the circuit diagram of the experiment of

302 lighting up the LEDs, when the TMG device generates positive current (Fig. S13a) and

303 negative current (Fig. S13b), respectively. The output end of the TMG device was

304 connected to an amplifier circuit (Circuit 1: yellow part), and the voltage regulator

305 circuit with external power supply was connected to the amplifier circuit to provide the

306 amplifier circuit with the energy required for amplification. As shown in Circuit 2 (blue

307 part), two LEDs in opposite directions were connected in parallel at the output end of

308 the amplifier circuit.

309   When the TMG device generates positive current, the red LED 1 conducts current

310 with a forward bias and it is turned ON, while the green LED 2 is OFF with a reverse

311 bias due to the unidirectional conduction characteristic of the diode (Fig. S13a).

312 Similarly, when the TMG device generates negative current, the red LED 1 is turned

313 off and the green LED 2 is lit (Fig. S13b).
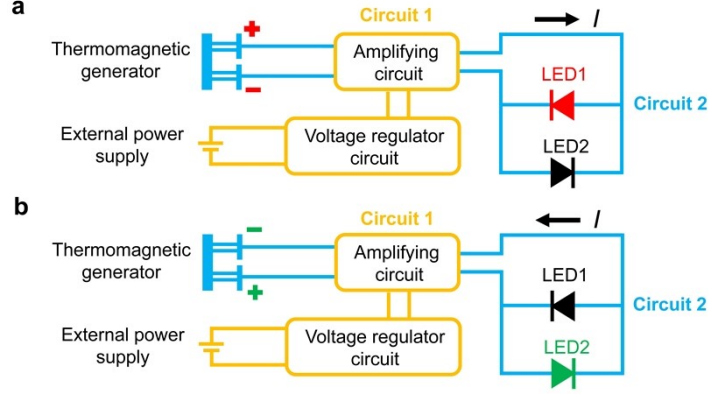
Fig. S13 The circuit diagram of the experiment of lighting up the LEDs, when the TMG generates (a) positive current and (b) negative current, respectively.

Supplementary Note 8. Relative energy conversion efficiency (η_{rel}) and the power density (P_D)

The relative energy conversion efficiency (η_{rel}) represents the ability of the Heusler alloys to convert thermal energy into electric energy during heating, which can be defined as the following equation:[9]

$$\eta_{rel} = \frac{\eta_{abs}}{\eta_{Carnot}} = \frac{\eta_{abs}}{1 - \dfrac{T_c}{T_h}} \tag{S8}$$

where $\eta_{Carnot} = 1 - T_c/T_h$ is the Carnot efficiency, T_c and T_h are the cold-end and hot-end temperatures, respectively. For our lab-built TMG device, the T_c and T_h are 289 K and 369 K, respectively, so the η_{Carnot} is 21.68%. η_{abs} is the absolute efficiency, which can be defined as:[9]

$$\eta_{abs} = \frac{E_{out}}{Q_{in}} \tag{S9}$$

where E_{out} is the net gain electric energy, which is expressed as:

$$E_{out} = \mu_0 H \Delta M \tag{S10}$$

where $\mu_0 H = 1$ T, ΔM is the magnetization change between T_c and T_h, and Q_{in} is the thermal energy absorbed by the sample, which is given by the following equation:[10-13]

$$Q_{in} = \rho \int_{T_c}^{T_h} C_P(T) dT \tag{S11}$$

333 where ρ is the density of sample, $C_P(T)$ is the heat capacity of sample. The Q_{in} is

334 determined by integrating the C_P–T curves in the working temperature range, as shown

335 in the shaded area in Fig. S14a-S14c. The blue region is the Q_{in} absorbed by the sample

336 during the FOMT, and the yellow region is the Q_{in} during the SOMT.

337   The thermal energy Q_{in} absorbed by the Heusler alloys during heating is

338 summarized in Fig. S14d. The total Q_{in} values of Co12.5, Co14, and NiMnIn alloys are

339 44.72 kJ kg^{-1}, 53.57 kJ kg^{-1}, and 35.57 kJ kg^{-1}, respectively. NiMnIn alloy shows the

340 lowest Q_{in}. According to equation (S9), this low Q_{in} of NiMnIn is favorable for higher

341 η_{abs} and η_{rel}.
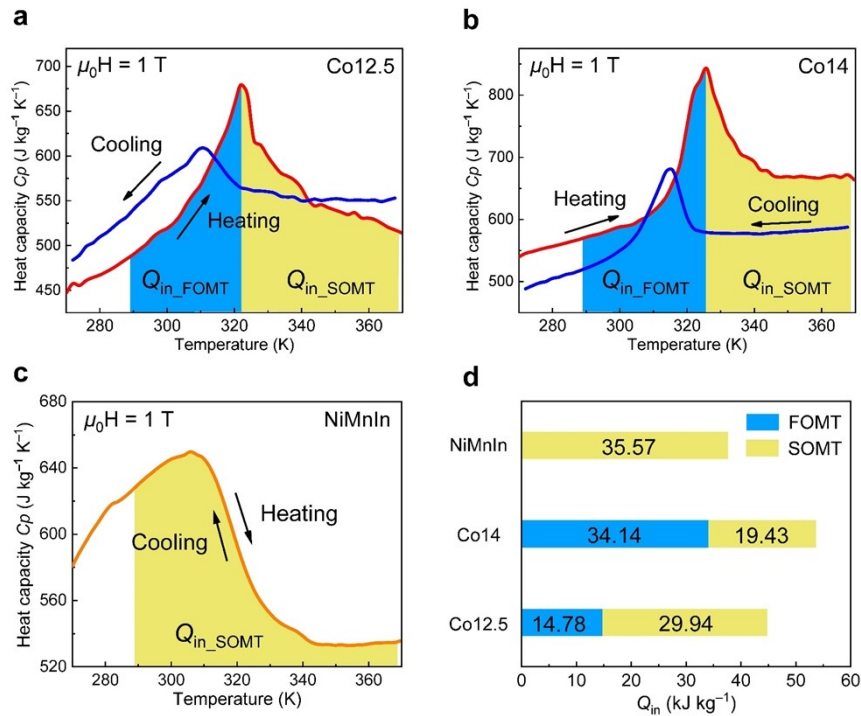
343 **Fig. S14** The calculation of Q_{in} based on C_P–T curves under 1 T for (a) Co12.5, (b) Co14, and (c)
344 NiMnIn, respectively. (d) The thermal energy Q_{in} absorbed by Heusler alloys during heating.

345   Fig. S15 compares the magnetization change ΔM during different phase transitions

346 in the heating process for all the alloys. For Co12.5 alloy, the ΔM during FOMT and

347 SOMT is 28 Am^2 kg^{-1} and 28 Am^2 kg^{-1}, respectively. For Co14 alloy, the ΔM during

348 FOMT and SOMT is 49 Am^2 kg^{-1} and 13 Am^2 kg^{-1}, respectively. On the other hand,

349 NiMnIn shows a high ΔM of 67 Am^2 kg^{-1} during the SOMT in the working temperature,

350 which is even higher than the total ΔM values of both FOMT and SOMT for Co12.5

351 (56 Am^2 kg^{-1}) and Co14 (62 Am^2 kg^{-1}) alloys. The higher ΔM value of NiMnIn is also

352 beneficial to obtain higher η_{abs} and η_{rel} according to the above equations.
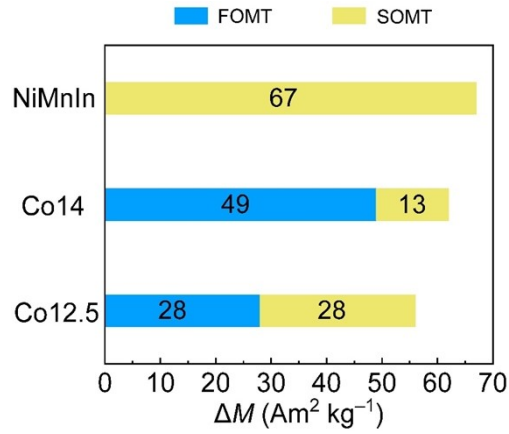
353

354 **Fig. S15** The magnetization change ΔM during different phase transitions in the heating process for
355 all the alloys.

356   Furthermore, the power density P_D evaluates the output electric power produced
357 by a unit volume of Heusler alloys.[12, 14] The maximum power density $P_{D\text{-max}}$ and
358 average power density $P_{D\text{-ave}}$ can be calculated as:

359
$$P_{D-max} = \frac{E_{max}^2}{RV} \tag{S12}$$

360
$$P_{D\text{-ave}} = \frac{\int_0^t V(t)^2 \, dt}{RVt} \tag{S13}$$

361 where E_{max} is the maximum induced voltage, R is the total resistance of system, V is the
362 volume of sample, $V(t)$ is the voltage variation over time t. NiMnIn alloy has the highest
363 $P_{D\text{-max}}$ (1752.3 mW m^{-3}), which is 3.3 and 1.6 times that of Co12.5 alloy (892.1 mW
364 m^{-3}) and Co14 alloy (1112.7 mW m^{-3}). Besides, NiMnIn alloy also has the highest $P_{D\text{-}}$
365 $_{ave}$ (0.50 μW cm^{-3}), which is 3.3 and 1.6 times that of Co12.5 alloy (0.15 μW cm^{-3}) and
366 Co14 alloy (0.32 μW cm^{-3}). This is mainly due to the highest V of the NiMnIn alloy
367 and the long peak duration time t as shown in Fig. 3a-3c in the main text.

368 Supplementary Note 9. Cost of the raw materials (*C*)

369   Fig. S16 shows the cost price of the raw materials obtained from Beijing Jiaming
370 Platinum Nonferrous Metals Co., Ltd. in 2023. The purity of Ni, Co, Mn, Ti, and In is

371 99.995 wt%, 99.98 wt%, 99.2 wt%, 99.995 wt%, and 99.995 wt%, respectively. The

372 cost index (C_0), which is defined as P_{D-max}/C, is used to evaluate the output power per

373 unit price. Here, we did not include the costs of processing and shaping in the present

374 analysis, as these costs depend on the scale of production. NiMnIn shows a relatively

375 higher C_0 of 2.78 µW €$^{-1}$ than that of Co12.5 (1.94 µW €$^{-1}$) and Co14 (2.43 µW €$^{-1}$),

376 which is mainly due to the highest P_{D-max} and low cost of NiMnIn alloy. Furthermore,

377 compared with other different material classes, as shown in Fig. 4g in the main text, the

378 C_0 of $Ni_2Mn_{1.4}In_{0.6}$ is 1–4 orders of magnitude higher than those of other typical

379 reported materials.
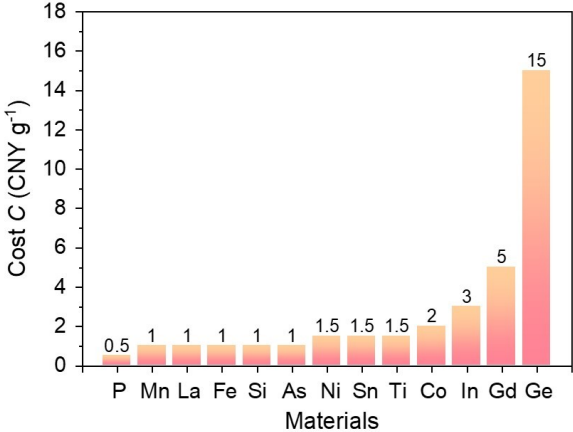
380

381 **Fig. S16** The costs of raw materials in this study.

Supplementary Note 10. Microstructure after long-term TMG service

383   Fig. S17 shows the SEM image of surface morphology for Heusler alloys after 450

384 heating and cooling cycles. Both Co12.5 alloy and NiMnIn alloy do not show any

385 cracks, but Co14 alloy develops obvious cracks after 450 cycles. This failure of Co14

386 alloy in long-term service is verified again in another Co14 sample (Co14-2). Since the

387 EDS maps have proved the uniform element distribution, the cracks are not caused by

388 inhomogeneous composition. The fracture of Co14 is caused by the accumulation of

389 dislocation and internal stress during the repetitive FOMT. In contrast, NiMnIn

390 undergoes a SOMT, and so presents superior service life without any cracks even after

391 1300 cycles.
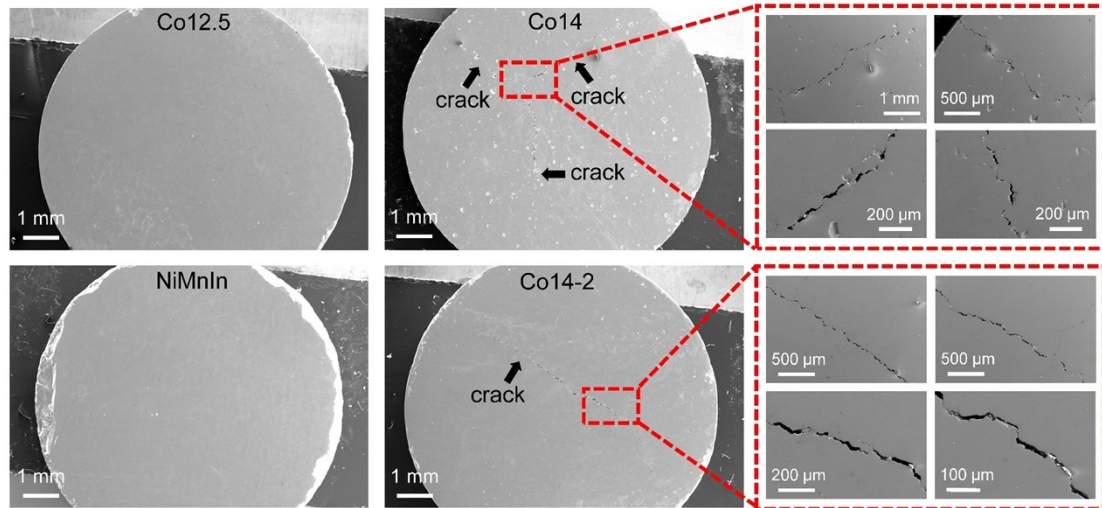
392

393 **Fig. S17** The SEM image of surface morphology for Heusler alloys after 450 heating and cooling
394 cycles.

395   Fig. S18 shows the scanning electron microscopy (SEM) images and the energy-
396 dispersive spectroscopy (EDS) maps for all the Heusler alloys. The EDS maps reveals
397 that the element distribution of all the alloys is uniform.
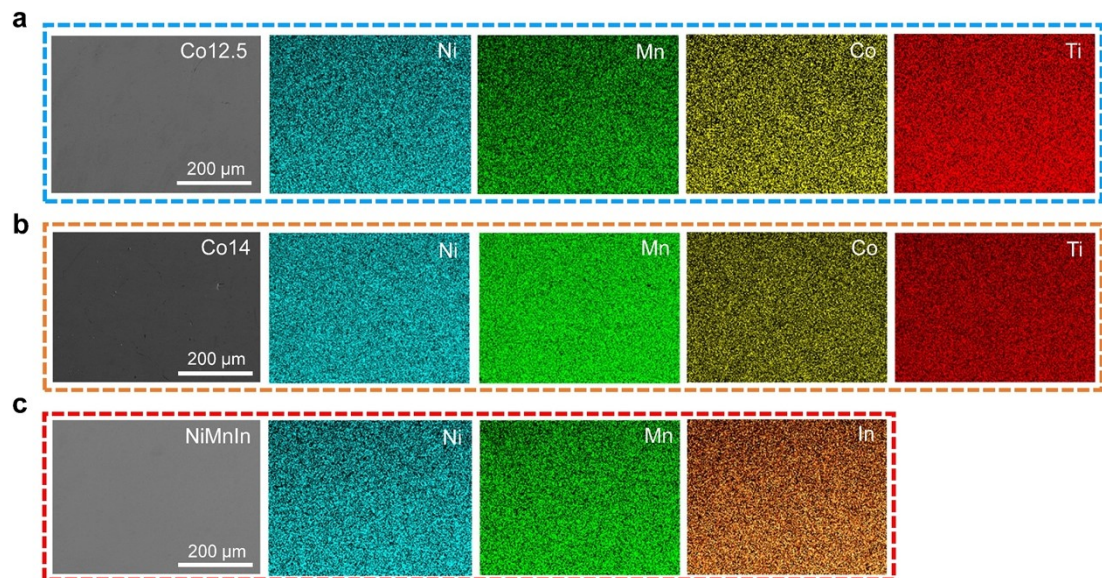
398

399 **Fig. S18** The SEM images and EDS maps for (a) Co12.5, (b) Co14, and (c) NiMnIn, respectively.

400   To further verify the long-term stability of SOMT NiMnIn material, we built a
401 cycle life test device and further extended the cycling time to 1 month (120,000 cycles).
402 Fig. S19a shows the cycle life test device. The sample is fixed on the rod of a slide rail,
403 and it can move up and down cyclically. A Peltier patch of ~288 K is placed above as
404 the heat sink, while a constant temperature water bath of ~363 K is placed below as the

heat source. The sample will be held for 3 s at each heating/cooling end in order to ensure the completion of the phase transition. As shown in Movie S4 (ESI†), the cooling and heating cycle of the sample was realized through the reciprocating motion of slide rail. As shown in Fig. S19b, SOMT NiMnIn material showed no cracks and maintained good cycling stability after 0, 1, 2, 3, 7, 14, 21, and 30 days of heating and cooling cycles. We also compared the SEM of the initial state and after 30 days (up to 120,000 cycles), and found that there is no significant difference between them (Fig. S19c). More importantly, we also tested the V–t curves of NiMnIn alloy after 0, 7, 14, 21, and 30 days, respectively, as shown in Fig. S19d. It shows that NiMnIn alloy maintains a very constant TMG performance, proving the excellent cycle stability of NiMnIn alloy with SOMT.
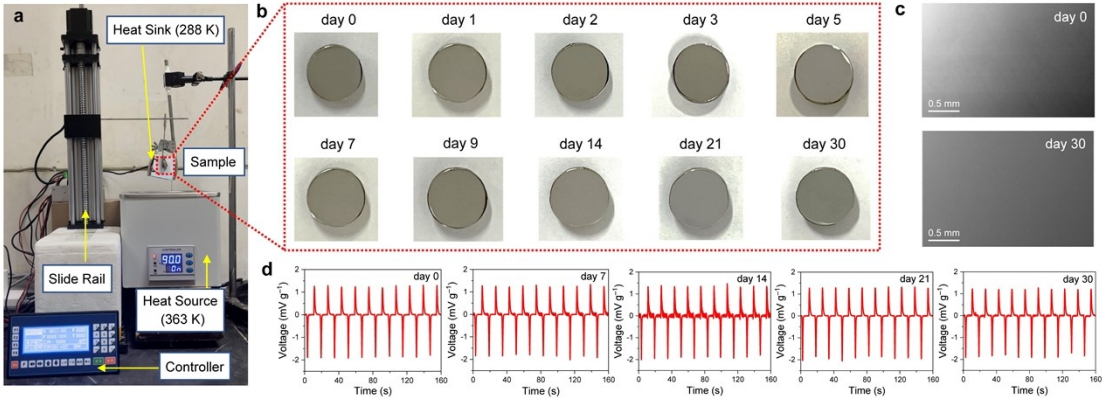
Fig. S19 (a) The cycle life test device. (b) The surface morphology of NiMnIn alloy after 0, 1, 2, 3, 7, 14, 21, and 30 days of heating and cooling cycles. (c) The SEM image of initial state and after 30 days of cooling and heating cycles of NiMnIn alloy. (d) The V–t curves of NiMnIn alloy after 0, 7, 14, 21, and 30 days of heating and cooling cycles.

Supplementary Note 11. Comparison between present work and other typical active TMGs

We summarized and compared the device and material parameters of our present work and other typical works based on the active TMG devices with traditional magnetic circuit, as shown in Table S2. The device parameters mainly include the temperature span ΔT, the total resistance of system R, the magnetic field H and the number of coil turns ω. The materials parameters mainly include the volume of sample V, the magnetization change during one cycle ΔM, the heat obsorbed during one heating

429 process Q_{in}, the density of sample ρ, the experimental current density I_0, the maximum

430 power density P_{D-max}, the average power density P_{D-ave}, and the relative energy

431 conversion efficiency η_{rel}.

432   Amomg them, parameters ΔT, R, H, ω, V, ΔM, ρ, and I_0 are all taken directly from

433 the corresponding references, Q_{in} is calculated by equation (S11), P_{D-max} is calculated

434 by equation (S12), P_{D-ave} is calculated by equation (S13), η_{rel} is calculated by equation

435 (2) in the main text, and PGI is calculated by equation (4) in the main text. The

436 comparison results show that our SOMT NiMnIn material has the highest P_{D-max}

437 (1752.3 mW m^{-3}) and C_0 (2.78 μW €$^{-1}$), which is 1–5 and 1–4 orders of magnitude

438 higher than those of most typical reported materials, respectively. In addition, we

439 proposed a new systematic comparison index, power generation index (PGI), which

440 takes into account the factors from both material and device that influence the induced

441 current. So, it can eliminate the comparison errors caused by various non-intrinsic

442 factors and is more reasonably to compare the TMG performance of different materials.

443 The PGI of NiMnIn is 1–7 orders of magnitude higher than those of other typical

444 reported materials. Consequently, the SOMT NiMnIn material shows an excellent

445 comprehensive TMG performance in comparison with other typical works based on the

446 active   TMG   devices   with   traditional   magnetic   circuit.

447 # **Supplementary Tables**

448 **Table S1** Relevant parameters for finite element simulations.

Parameter	Value	Uint
Initial test temperature	289	K
Cold fluid temperature	289	K
Hot fluid temperature	369	K
Fluid velocity	0.04	$L\ s^{-1}$
Time of one cycle	16	s
Turns of the coil	600	
Inside radius of the coil	0.97	cm
Outside radius of the coil	2.31	cm
Length of the coil	1.24	cm
Diameter of the wire	0.04	cm
Inside radius of the permanent magnet	4.4	cm
Outside radius of the permanent magnet	11.2	cm
Height of the permanent magnet	20	cm
Applied magnetic field	1	T
Resistance of the coil	6.7	Ω
Coercivity of the permanent magnet	1037	$kA\ m^{-1}$
Relative permeability of the permanent magnet	1.056	

450 **Table S2** Comparison of the device and materials parameters of this work with other works based on the active TMG devices with traditional magnetic circuit. The
451 device parameters include the temperature span ΔT, the total resistance of system R, the magnetic field H and the number of coil turns ω. The materials parameters
452 include the volume of sample V, the magnetization change during one cycle ΔM, the heat absorbed during one heating process Q_{in}, the density of sample ρ, the current
453 density I_0, the power generation index PGI, the maximum power density P_{D-max}, the average power density P_{D-ave}, and the relative energy conversion efficiency η_{rel}.

Alloy [Ref]	ΔT (K)	R (Ω)	H (T)	ω	V (cm^{-3})	ΔM (Am^2 kg^{-1})	Q_{in} (kJ kg^{-1})	ρ (kg m^{-3})	I_0 (μA g^{-1})	PGI $\times 10^{-6}$	P_{D-ave} (mW m^{-3})	P_{D-max} (mW m^{-3})	η_{rel} $\times 10^{-4}$ (%)
Ni$_2$Mn$_{1.4}$In$_{0.6}$	80	6.7	1	600	0.314	67	35.57	7935	286.57	891.08	500.68	1752.26	1.09
(Mn, Fe)$_2$(P, As) [15]	16	47.02	0.24	240	4.89	n/a	n/a	n/a	5.53	127.61	9.90	53.28	n/a
Phytherm 55 alloy [16]	60	102.2	0.4	400	1.925	32	25.20	8100	76.92	78.40	0.97	7.32	0.33
Ni$_{45}$Co$_5$Mn$_{40}$Sn$_{10}$ [17]	300	10000	0.2	2000	0.375	137.5	129.00	8000	0.02	1.67$\times 10^{-5}$	0.03	0.10	0.06
Gd-1 [8]	85	15	1.3	300	0.786	67	23.49	7610	22.58	45.41	52.16	471.25	2.07
Gd-2 [2]	65	15	1	300	0.786	42	15.62	7610	4.82	16.48	0.10	31.72	1.92
La(Fe, Si)$_{13}$H$_y$/In [2]	65	15	1	300	0.786	59	25.23	6500	9.12	31.18	0.42	53.05	1.95
Gd$_5$(Si, Ge)$_4$ [1]	65	15	1	300	0.786	50	25.48	7010	4.28	14.63	0.13	21.22	1.52
Ni$_{50}$Mn$_{34}$Co$_2$Sn$_{14}$ [1]	65	15	1	300	0.786	26	26.95	7960	2.37	8.10	0.05	8.39	0.66
Mn$_{1.2}$Fe$_{0.8}$P$_{0.4}$Si$_{0.6}$ [18]	~70	167.2	0.553	1500	10.33	20	35.82	4842	1.3	0.13	n/a	68.39	0.32
Mn$_{1.2}$Fe$_{0.8}$P$_{0.35}$Si$_{0.65}$ [19]	~90	~105	0.8	2700	26.64	17.5	46.06	4879	0.62	0.03	n/a	25.23	0.26
Fe$_{62.3}$Ni$_{37}$Mn$_{0.4}$Si$_{0.3}$ [20]	10	200	~0.3	2000	n/a	n/a	n/a	n/a	22.69	18.91	n/a	n/a	n/a

Notes and references

1   H. Chen, Z. Ma, X. Liu, K. Qiao, L. Xie, Z. Li, J. Shen, W. Dai, Z. Ou, H. Yibole, O. Tegus, S. V. Taskaev, K. Chu, Y. Long and H. Zhang, *Appl. Energy*, 2022, **306**, 117999.

2   Z. Ma, H. Chen, X. Liu, C. Xing, M. Wu, Y. Wang, P. Liu, Z. Ou, J. Shen, S. V. Taskaev, K. Long, Y. Long and H. Zhang, *Adv. Sustainable Syst.*, 2021, **5**, 2000234.

3   D. D. Viehland and E. K. H. Salje, *Adv. Phys.*, 2014, **63**, 267-326.

4   K. Liu, X. Han, K. Yu, C. Ma, Z. Zhang, Y. Song, S. Ma, H. Zeng, C. Chen, X. Luo, S. U. Rehman and Z. Zhong, *Intermetallics*, 2019, **110**, 106472.

5   Z. Wei, E. Liu, J. Chen, Y. Li, G. Liu, H. Luo, X. Xi, H. Zhang, W. Wang and G. Wu, *Appl. Phys. Lett.*, 2015, **107**, 022406.

6   T. Krenke, E. Duman, M. Acet, E. F. Wassermann, X. Moya, L. Manosa and A. Planes, *Nat. Mater.*, 2005, **4**, 450-454.

7   X. Liu, H. Chen, J. Huang, K. Qiao, Z. Yu, L. Xie, R. V. Ramanujan, F. Hu, K. Chu, Y. Long and H. Zhang, *Nat. Commun.*, 2023, **14**, 4811.

8   X. Liu, H. Zhang, H. Chen, Z. Ma, K. Qiao, L. Xie, Z. Ou, J. Wang, F. Hu and B. Shen, *Appl. Therm. Eng.*, 2023, **221**, 119827.

9   R. A. Kishore and S. Priya, *Renewable Sustainable Energy Rev.*, 2018, **81**, 33-44.

10 L. D. Kirol and J. I. Mills, *J. Appl. Phys.*, 1984, **56**, 824-828.

11 D. Solomon, *J. Appl. Phys.*, 1988, **63**, 915-921.

12 M. Gueltig, F. Wendler, H. Ossmer, M. Ohtsuka, H. Miki, T. Takagi and M. Kohl, *Adv. Energy Mater.*, 2017, **7**, 1601879.

13 Y. T. Song, K. P. Bhatti, V. Srivastava, C. Leighton and R. D. James, *Energy Environ. Sci.*, 2013, **6**, 1315-1327.

14 M. Gueltig, H. Ossmer, M. Ohtsuka, H. Miki, K. Tsuchiya, T. Takagi and M. Kohl, *Adv. Energy Mater.*, 2014, **4**, 1400751.

15 T. Christiaanse and E. Brück, *Metall. Mater. Trans. E*, 2014, **1**, 36-40.

16 M. Lallart, L. Wang, G. Sebald, L. Petit and D. Guyomar, *Phys. Lett. A*, 2014, **378**, 3151-3154.

17 V. Srivastava, Y. Song, K. Bhatti and R. D. James, *Adv. Energy Mater.*, 2011, **1**, 97-104.

18 L. Bi, O. Tegus, R. Yi and H. Shi, *Acta Phys. Sin.*, 2012, **61**, 077103.

19 Z. Liu, O. Tegus, Z. Ou, W. Fan, Z. Song, H. Lu, W. Wei and R. Han, *Acta Phys. Sin.*, 2015, **64**, 047103.

20 J. Liu, Y. Long, D. Bai, H. Sun, H. Zhang, K. Long and T. Yan, *AIP Adv.*, 2019, **9**, 045227.